

Cite this: *J. Mater. Chem. A*, 2025, **13**, 10487

Orientation control (horizontal and vertical) of TiO₂ single-crystalline nanowire arrays for high-performance gas sensing: a surface supersaturation-driven approach†

Chen-Hu Shen,^{ad} Wen-Jing Jiang,^c Yong-Jun Chen,^a Guan-E. Wang,^{id ab} Gang Xu^{id *ab} and Xiao-Liang Ye^{*a}

In the field of advanced functional nanoarrays, the development of one-dimensional (1D) single-crystalline nanoarrays (SCNAs) with highly orientated alignment is of paramount significance owing to their essential roles in batteries, catalysis, and sensing applications. However, tuning SCNAs to ensure a uniform orientation is extremely challenging. Herein, a surface supersaturation-driven hydrothermal growth approach that could successfully modulate the growth directions of TiO₂ nanowires is proposed. By precisely tuning the concentrations of the crystal seed solution, a series of highly aligned TiO₂ SCNAs was obtained, which was grown horizontally (TiO₂-H-NAs) or vertically (TiO₂-V-NAs) on sapphire. Compared with TiO₂-V-NAs, TiO₂-H-NAs displayed better sensing performance towards ethanol at room temperature, which represents one of the highest responses among various other material categories, including metal oxide semiconductors, metal–organic frameworks, 2D materials and polymers. Demonstrating their practical utility, TiO₂-H-NAs showcased an obvious response value (288%) in an exhalation breath testing after wine consumption, underscoring their potential in real-time monitoring applications. This study offers a promising pathway to overcome the synthetic challenges and unlock the full potential of 1D nanowires for various chemical applications.

Received 21st January 2025
Accepted 2nd March 2025

DOI: 10.1039/d5ta00573f

rsc.li/materials-a

Introduction

As novel and distinct assembled structures of nanomaterials, single-crystalline nanoarrays (SCNAs) with highly preferred orientation have been extensively investigated, among which one-dimensional (1D) SCNAs (nanowire arrays, nanorod arrays, *etc.*) have attracted tremendous interest because of the significant advantages they offer in the realm of catalysis, energy, and sensing.^{1–6} Owing to their effective electron transport and superior mass transfer, 1D SCNAs are regarded as ideal materials for chemical applications, particularly exhibiting unprecedented potential in various optoelectronics and sensing applications.^{7–10}

Orientation control of 1D SCNAs has a crucial impact on their chemical and physical properties.^{11,12} In some cases, compared with vertical nanoarrays (V-NAs), regular horizontal nanoarrays (H-NAs) could provide more electron-transport channels and stronger interactions between nanowires and the reactant.^{13,14} As a result, the accelerated electron conduction and increased mass transfer would promote the higher performance of 1D SCNAs grown horizontally.¹⁵ Conventional techniques, including hydrothermal methods, chemical vapor deposition and electrochemical deposition, have been developed to prepare vertical 1D SCNAs.^{16–20} However, H-NAs are more difficult to fabricate on account of the need to limit the competitive growth in other directions, which would require special catalyst assistance or surface modification.^{21–23} Unfortunately, even with careful control of experimental parameters and the ambient environment, the chaotic alignment of nanowires will normally occur during fabrication using traditional synthetic methods.^{24,25} This severely hinders the application of H-NAs in micro–nanoelectronic devices and rigid integrated chips.^{26,27} Therefore, a fast and facile method to fabricate stable and highly ordered H-NAs with a uniform orientation (or growth direction) and regular alignment is desirable.

In this work, we report a surface supersaturation-driven hydrothermal growth approach for constructing highly

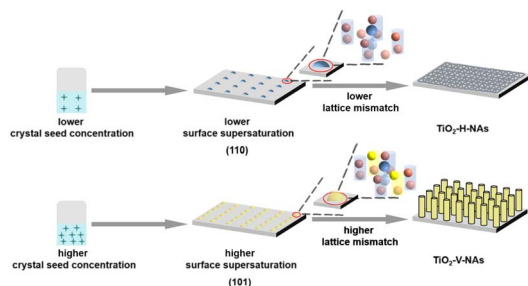
^aState Key Laboratory of Structural Chemistry, Fujian Institute of Research on the Structure of Matter, Chinese Academy of Sciences (CAS), Fuzhou, Fujian, 350002, P. R. China

^bFujian College, University of Chinese Academy of Sciences, Fuzhou City, Fujian, 350002, China

^cFujian Science & Technology Innovation Laboratory for Optoelectronic Information of China, Fuzhou City, Fujian, 350108, P. R. China

^dUniversity of Chinese Academy of Science (UCAS), Beijing 100049, China

† Electronic supplementary information (ESI) available: Synthetic details. See DOI: <https://doi.org/10.1039/d5ta00573f>



Scheme 1 Schematic showing the TiO_2 nanoarray growth utilizing a surface supersaturation-driven approach.

aligned H-NAs and V-NAs from TiO_2 nanowires (Scheme 1). According to the Ostwald–Freundlich equation, during crystal seed concentration-assisted nucleation, lower crystal seed supersaturation would guarantee exposure of the crystal facet with a lower surface energy (110). Next, during the hydrothermal growth, single-crystalline nanowires would preferentially grow along the direction with minimum lattice mismatch, which would lead to the horizontal growth of NAs and their assembly into regular H-NAs. By finely decreasing the surface supersaturation of crystal seed concentrations from 0.06 to 0.04 M, the growth direction of TiO_2 nanowires could be exquisitely regulated from V-NAs to H-NAs. The effects of the different assembled TiO_2 nanowires (TiO_2 -H-NAs and TiO_2 -V-NAs) on the gas-sensing performance were carefully investigated. It was found that, compared with TiO_2 -V-NAs, TiO_2 -H-NAs presented better sensing performance. Meanwhile, the chemiresistive gas sensor fabricated with TiO_2 -H-NAs demonstrated the highest sensitivity, with a response of 2450% to 10 ppm ethanol and an ultra-low limit of detection (0.6 ppb), suggesting that it is one of the best room temperature ethanol sensing materials reported to date.

Results and discussion

Morphological and structural characterization

In this study, we developed a two-step approach for synthesizing TiO_2 NAs. The process involved the following key steps. First, a layer of tetrabutyl titanate was spin-coated onto a sapphire substrate, followed by sintering to form TiO_2 nuclei. This step provided the base for the subsequent growth of the NAs. Next, utilizing a simple hydrothermal method, TiO_2 NAs were grown horizontally on crystal nuclei with a mixed solution of hydrochloric acid and tetrabutyl titanate. The samples prepared under various supersaturations (0.02–0.06 M) were labeled as A1–A5 (see ESI† for details). For the convenience of subsequent description, the samples A3 and A5 were also named as TiO_2 -H-NAs and TiO_2 -V-NAs, respectively.

PXRD patterns illustrated that the synthesized TiO_2 was the rutile type, with all diffraction peaks consistent with the PDF report (no. 21-1276). Peaks centered at 27.4° and 36.1° corresponded to the (110) and (101) facets of TiO_2 , respectively, presenting the dominant facets of the rutile structure.^{28,29} For TiO_2 -H-NAs, two peaks were observed at 27.4° and 56.6° ,

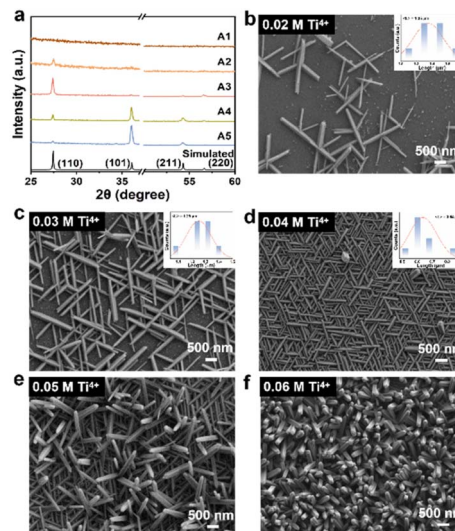


Fig. 1 (a) PXRD patterns of TiO_2 with different crystal seed concentrations. SEM images of TiO_2 for (b) 0.02, (c) 0.03, (d) 0.04, (e) 0.05 and (f) 0.06 M Ti^{4+} (insets show the length distributions of the TiO_2 nanowires).

corresponding to the (110) and (220) crystal facets (pattern of A3 in Fig. 1a), respectively, revealing that TiO_2 -H-NAs grew along the (110) crystal plane. In contrast, for TiO_2 -V-NAs, three peaks at 27.4° , 36.1° , and 54.3° , assigned to the (101), (110) and (211) crystal facets (pattern A5 in Fig. 1a), respectively, were observed, suggesting that TiO_2 -V-NAs grew along the (101) crystal plane.

As illustrated in Fig. 1b, when keeping the concentration of the precursor constant, TiO_2 nanowires (sample A1) with a diameter of 100 ± 10 nm were grown horizontally at a low $\text{Ti}(\text{iv})$ seed concentration (0.02 M). SEM images show that as the $\text{Ti}(\text{iv})$ concentration increased, the nanowire density transitioned gradually from sparse to dense (Fig. 1c). When the $\text{Ti}(\text{iv})$ concentration reached 0.04 M, the TiO_2 NAs (sample A3, with a diameter of 100 nm) grew horizontally and were arranged in a regular alignment of triangles on the substrate (Fig. 1d). Meanwhile, the cross-sectional SEM image of sample A3 (Fig. S1a†) showed that the thickness of TiO_2 -H-NAs was about 100 nm, revealing the quasi single-layer-stacking of NAs. However, when the concentration reached 0.05 or 0.06 M, due to the high strain energy (discussed in the section covering the growth mechanism), the TiO_2 nanowires gradually grew vertically to form V-NAs on the sapphire substrate (Fig. 1e and f). Besides, the lengths of the above TiO_2 nanowires were recorded. As shown in Fig. 1, the average lengths of A1, A2 and A3 were 1.35, 1.25 and 0.64 μm , respectively. Moreover, the length of TiO_2 -V-NAs (sample A5) was about 2.6 μm , according to the cross-section SEM image of sample A5 (Fig. S1b†).

Fig. 2a and b present the TEM images of TiO_2 -H-NAs and TiO_2 -V-NAs, with lattice fringes of 0.32 and 0.25 nm corresponding to the (110) and (101) facets, respectively. Moreover, the (110) and (101) crystal facets could be clearly seen in the fast Fourier transformed images (insets of Fig. 2a and b). These results were consistent with the PXRD analysis (Fig. 1a).

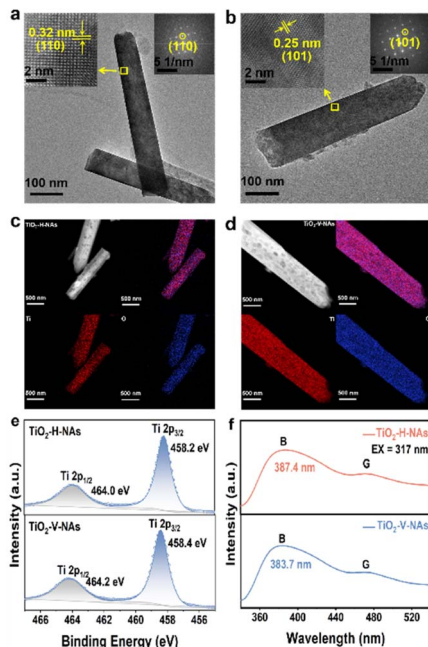


Fig. 2 TEM images of (a) TiO_2 -H-NAs and (b) TiO_2 -V-NAs (inset show the lattice fringes and fast Fourier transformed patterns). STEM-EDS mapping of (c) TiO_2 -H-NAs and (d) TiO_2 -V-NAs. (e) High-resolution XPS spectra of TiO_2 -H-NAs and TiO_2 -V-NAs in the Ti 2p region. (f) Photoluminescence of TiO_2 -H-NAs and TiO_2 -V-NAs.

Meanwhile, STEM-EDS elemental mapping diagrams of TiO_2 -H-NAs and TiO_2 -V-NAs (Fig. 2c and d) illustrate that Ti and O elements were both well distributed throughout the nanowires.

XPS analysis was performed to investigate the elemental and chemical composition of the surface of TiO_2 -H-NAs and TiO_2 -V-NAs. From survey XPS spectra (Fig. S2†), peaks of Ti, O, and C could be observed, which were in accordance with the STEM-EDS results. In the Ti 2p spectrum (Fig. 2e) for TiO_2 -H-NAs, peaks located at 458.2 eV and 464.0 eV could be observed, corresponding to Ti 2p_{3/2} and Ti 2p_{1/2}, respectively. These two peaks were derived from Ti^{4+} of TiO_2 with a binding energy difference of 5.8 eV.^{30,31} Meanwhile, after careful XPS analysis of the TiO_2 nanowires, it was found that the valence states of Ti on TiO_2 -H-NAs and TiO_2 -V-NAs were maintained during growth orientation modulation (Fig. 2e).

Photoluminescence (PL) spectroscopy is an essential characterization tool for studying defects.³² The PL spectra of TiO_2 -H-NAs and TiO_2 -V-NAs were measured from 340 to 540 nm with an excitation wavelength of 317 nm (Fig. 2f). Two main peaks appeared for TiO_2 -H-NAs and TiO_2 -V-NAs: peak B, located in the UV region, was related to the electronic transition from the conduction band to the valence band,³³ while peak G in the visible region was attributed to the band-edge free excitons and bound excitons.³⁴ These excitons represent surface defects and oxygen vacancy-related trap-assisted recombination.³⁵ The intensity ratio of peak G and peak B (I_G/I_B) indicated the presence of trap-related defects.^{36,37} Compared with TiO_2 -V-NAs (383.7 nm), peak B of TiO_2 -H-NAs (387.4 nm) was red-shifted by 3.7 nm, revealing a relative increment in oxygen vacancies

and a reduction in the band gap in TiO_2 -H-NAs. Meanwhile, the I_G/I_B of TiO_2 -H-NAs (0.63) was higher than that of TiO_2 -V-NAs (0.59), which further suggested that there were more defects in TiO_2 -H-NAs than in TiO_2 -V-NAs. Besides, similar results were obtained from Raman analysis, which was performed on a LabRAM HR system (see details in the ESI, Fig. S3†).

Possible formation process and growth mechanism

The surface energy of TiO_2 for the (110) and (101) facets was 0.42 and 0.98 J m⁻², respectively.³⁸ Consequently, at atmospheric pressure, TiO_2 exists in the most stable tetragonal rutile structure with the thermodynamically stable (110) facet as the dominant facet.³⁹ Moreover, we found that by varying the supersaturation of the crystal seed, the crystal facet orientation and different growth directions could be well modulated.

To reveal the crystal facet orientation mechanism of the TiO_2 NAs, the Ostwald–Freundlich equation in thermodynamics (eqn (1)) was quoted.

$$\frac{2\gamma v}{r} = k_B T \ln S \quad (1)$$

In our case, in the early stage of crystal seed-assisted nucleation, a lower crystal seed concentration (0.04 M Ti^{4+}) was used to reduce the supersaturation (S) of the crystal nuclei on the substrate, which led to a decrease in the surface energy (γ). As shown in Fig. 3a, TiO_2 crystal nuclei (red dashed circles, with a size of 1.95 nm, see the inset of Fig. 3a) could be clearly observed, with an exposed low γ crystal facet (110). On the

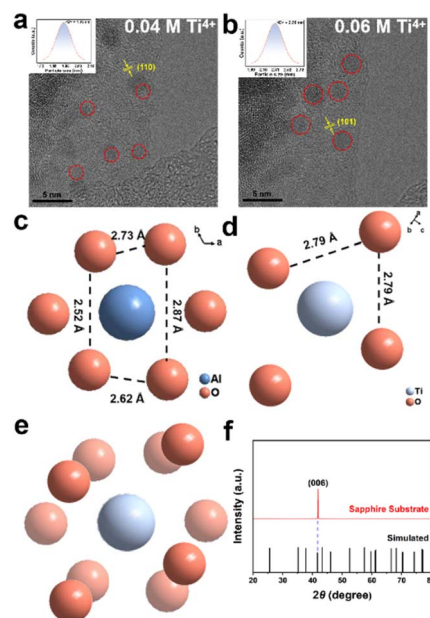


Fig. 3 Crystal faces exposed by TiO_2 nuclei formed from different crystal seed concentrations. (a) 0.004 M Ti^{4+} and (b) 0.04 M Ti^{4+} (the red circles indicate TiO_2 nuclei; insets show the particle sizes of the TiO_2 nuclei). Schematic plots of the lattice relationships between the sapphire substrate and TiO_2 -H-NAs. (c) Sapphire substrate (006), (d) TiO_2 -H-NAs (110) and (e) TiO_2 -H-NAs (110) on the sapphire substrate (006). (f) PXRD of the sapphire substrate.

contrary, at a high crystal seed concentration (0.06 M Ti^{4+}), S of the crystal nuclei on the substrate improved. Therefore, the higher γ crystal facet (101) of TiO_2 crystal nuclei (Fig. 3b) with a size of 2.30 nm gradually appeared.⁴⁰

Next, during the hydrothermal growth of the same crystal, strain energy was generated owing to the lattice mismatch at the interface between the crystal and the substrate.⁴¹ Here, the crystals would preferentially grow along the direction with the minimum strain energy.^{42,43} Therefore, the lattice mismatch between the two types of TiO_2 NAs and sapphire was carefully explored. As shown in Fig. 3c–e, the oxygen atomic arrangements between the sapphire (006) (Fig. 3f) plane and TiO_2 (110) plane (the low γ facet) were similar, revealing the least strain energy. As a result, when lower seed supersaturation was used, the TiO_2 NAs would grow horizontally along the (110) direction with minimized lattice mismatch values of 2.20% and -2.79% along the sapphire [100] and [120] planes, respectively. However, with an increase in crystal seed supersaturation, the (101) crystal facet appeared (Fig. 3b). The difference in oxygen atomic arrangements between the sapphire (006) plane and TiO_2 (101) plane (Fig. S4†) caused an increase in the strain energy. Hence, the TiO_2 NAs would grow vertically along the direction with the lower energy.

Sensing performance

To demonstrate the gas-sensing performance by regulating the arrangement of nanowires, various TiO_2 samples (A1–A5) were fabricated as chemiresistive sensors and evaluated at room temperature on our homemade test system.⁵ Upon light assistance, the overall performance of the TiO_2 nanowires was optimized by adjusting the growth orientation (sensors A1 were disconnected due to the sparsity of nanowires). As with the NAs grown densely on the substrate, the sensors fabricated with sample A2 presented obvious response values of 507% and 378% towards 10 ppm ethanol and methanol, respectively

(Fig. 4a). Furthermore, TiO_2 -H-NA sensors (sample A3) exhibited the highest response to 10 ppm ethanol with an average value of $2453\% \pm 33\%$. It was worth nothing that the response value towards 10 ppm ethanol was 3.2 times higher than that towards 10 ppm methanol, revealing the higher selectivity of TiO_2 -H-NA sensors towards ethanol than methanol. When further increasing the Ti(IV) concentration, the sensor made with A5 with the TiO_2 NAs on the sapphire substrate showed a decreased response value towards 10 ppm ethanol (619%) and decreased selectivity towards ethanol.

Since the selectivity of the TiO_2 -H-NA sensor towards ethanol was higher than that of methanol, we took the sensing performance toward ethanol for the sensors of TiO_2 -H-NAs as an example. The performance toward methanol is discussed in the ESI (Fig. S5†). As shown in Fig. 4b, upon cyclic exposure to ethanol with a concentration ranging from 2 to 100 ppm, the currents of TiO_2 -H-NAs sensor increased rapidly but then recovered to the initial value when purged with dry air, revealing their excellent reversibility. Meanwhile, the responses to 10 ppm ethanol for 3 continuous cycles was maintained with a low coefficient of variation ($\text{CV} = 1.3\%$), indicating the good cycle stability of the sensors (for TiO_2 -V-NAs, please see Fig. S6†). Furthermore, the response–concentration log–log plots of the prepared devices presented superior linearity, suggesting their potential application in ethanol detection and analysis (Fig. 4c). By setting the response value to 10%, an ultra-low theoretical limit of detection (LOD) could be calculated as 0.6 ppb for TiO_2 -H-NAs, which was twice as low as that of TiO_2 -V-NAs. Notably, as illustrated in Fig. 4d, the response–LOD plot suggested that TiO_2 -H-NAs are one of the best sensors among all the reported room temperature ethanol sensing materials, including metal oxide semiconductors, metal–organic frameworks, 2D materials (graphene-based materials, graphitic carbon nitride, transition metal chalcogenides and MXenes) and polymers (Table S1†).

Devices fabricated using TiO_2 -H-NAs showed not only high sensitivity in a broad detection range (2–100 ppm), but also extraordinary selectivity. To investigate this, 14 interferences were selected to evaluate the selectivity of TiO_2 -H-NA sensors. TiO_2 -H-NAs exhibited responses below 200% towards all the 14 interfering gases (Fig. 4e), with the selectivity coefficients ranging from 49 to 1231 (Fig. S7†). In addition, the response of TiO_2 -H-NAs towards ethanol remained above 85% after 120 days, disclosing their outstanding long-term stability (Fig. 4f). Besides, the effect of relative humidity (RH) on the gas response to 10 ppm EtOH was carefully studied (see details in Fig. S8†).

Sensing mechanism

The exact ethanol sensing mechanism of TiO_2 -H-NAs remains unclear. However, comparison between the sensing performances of TiO_2 -H-NAs and TiO_2 -V-NAs helped elucidate the key role of the horizontally grown, regularly arranged 1D SCNAs in the high sensing performance. As mentioned above, active oxygen species are the reactants for the sensing reaction, and their concentration on the surface of the sensing materials significantly affects their sensitivity.^{44–47} XPS measurements

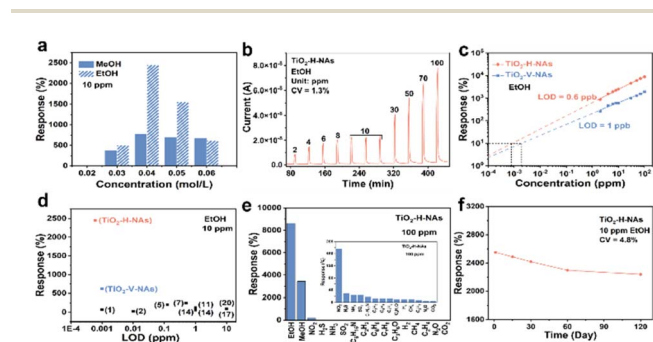


Fig. 4 (a) Response comparison of samples with different TiO_2 precursor concentrations to 10 ppm ethanol and methanol. (b) Response–recovery curve to ethanol with different concentrations (2–100 ppm) of TiO_2 -H-NAs. (c) Log–log linear fitting of the response–concentration plot for ethanol. (d) Response–LOD relationship compared with some reported ethanol sensing materials (including metal oxide semiconductors, metal–organic frameworks, 2D materials and polymers). (e) TiO_2 -H-NAs' sensing performance in the presence of different interfering gases at a concentration of 100 ppm. (f) Long-term stability of TiO_2 -H-NAs to 10 ppm ethanol.

revealed the O 1s spectra of TiO₂-H-NAs and TiO₂-V-NAs deconvoluted into three major subpeaks corresponding to lattice oxygen (O_{latt}, 529.5 and 529.7 eV) and adsorbed active oxygen species (O_{ads}, 530.3 and 530.4 eV, mainly O₂⁻ at RT), respectively (Fig. 5a). The relative percentage of O_{latt}, O_{ads} is illustrated in Fig. 5a. Notably, with less nanowires compared with that in TiO₂-V-NAs, TiO₂-H-NAs showed much higher efficiency in increasing O_{ads} with a value as high as 51.67%, which was in accordance with the Raman results (Fig. S3†) and PL spectral analysis (Fig. 2f).

Similar to the cases in other reported n-type sensing materials, the relevant mechanism could be explained by the surface-depletion model and Wolkenstein adsorption-desorption theory,^{48,49} which are discussed in the ESI.† Here, relevant verification was carried out with *in situ* near ambient pressure X-ray photoelectron spectroscopy (NAP-XPS). Briefly, at the start of the sensing (region I), TiO₂-based devices captured electrons from the atmosphere to form O₂⁻ (Fig. S9†). When the devices were exposed to an ethanol atmosphere (region II), ethanol molecules could be absorbed on TiO₂ NAs, which would react with O₂⁻ to form carbon dioxide.^{50–52} Carbon dioxide molecules were confirmed by the observable peaks located in the C 1s (291.9 eV) and O 1s (537.6 eV) spectra before and after ethanol treatment (Fig. 5b and S9†).^{53,54} After the target analyzing gas was removed, O₂ adsorbed onto the TiO₂ NAs again, recovering its highly resistive state (region III in Fig. 5c).

Based on the above experimental results, it could be seen that the sensing performance towards ethanol was one of the highest reported for chemiresistive sensors in a broad concentration range (Fig. 6a). Considering their high sensitivity and excellent selectivity with an ultra-low LOD, it could be inferred that the developed TiO₂-H-NA sensors would be viable for rapid ethanol breath testing. As a proof of concept, an actual environment was simulated (Fig. 6b) for exhalation detection by directly purging the device with 100 ppm ethanol for 5 continuous cycles (see the details in the ESI Videos†), which exhibited

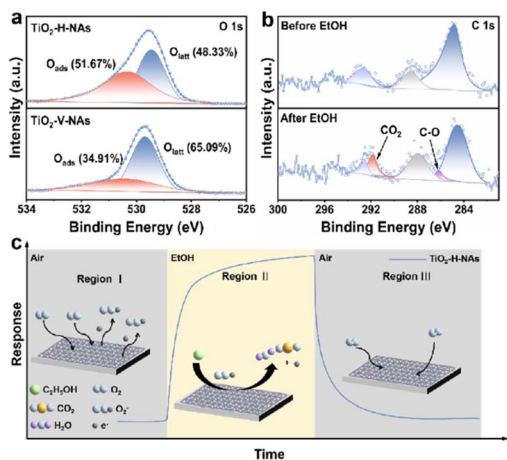


Fig. 5 (a) High-resolution XPS spectra of TiO₂-H-NAs and TiO₂-V-NAs in the O 1s region. (b) *In situ* NAP-XPS spectra of TiO₂-H-NAs for C 1s recorded with 5 mbar air (before EtOH) and 5 mbar gas mixtures of 1000 ppm EtOH (after EtOH). (c) Proposed ethanol sensing mechanism for TiO₂-H-NAs.

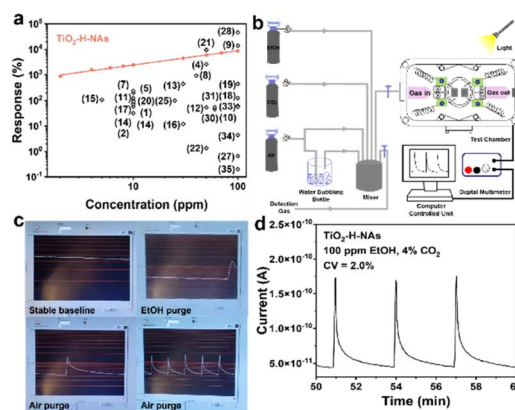


Fig. 6 (a) Response–concentration relationship compared with some reported ethanol sensing materials (including metal oxide semiconductors, metal–organic frameworks, 2D materials and polymers). (b) Diagram showing the simulation detection of ethanol exhalation. (c) Images of the simulated experimental processes. (d) Testing cycles repeated thrice by blowing the device directly with 100 ppm ethanol.

their reliable stability (Fig. 6c). Notably, by purging directly with 100 ppm ethanol, an obvious real-time response (Fig. 6d) was obtained, which would undoubtedly meet the requirements for practical application.⁵⁵

Conclusions

In summary, this study successfully developed a surface supersaturation-driven hydrothermal growth approach for designing novel 1D SCNAs with a highly orientated horizontal and vertical alignment. This method overcomes the critical challenge of enhancing the regularity of the growth direction without compromising the horizontal growth of nanowires. Accordingly, TiO₂-H-NAs, a material that exhibits one of the highest room temperature response levels with an ultra-low LOD compared with all reported chemiresistive materials for ethanol sensing, were fabricated. As an exemplary application, TiO₂-H-NAs demonstrated a rapid response to 100 ppm ethanol, which indicates their potential for use in exhalation tests after alcohol consumption. The proposed new strategy offers a pathway to enhance the functionality of 1D NAs for diverse applications, particularly in the field of chemical sensing.

Data availability

The data supporting this article have been included as part of the ESI.†

Conflicts of interest

There are no conflicts to declare.

Acknowledgements

This work was supported by the National Natural Science Foundation of China (22325109, 22171263, 62227815, 91961115 and 22203013), Scientific Research and Equipment

Development Project of CAS (YJKYQ20210024), the Natural Science Foundation of Fujian Province (2021J02017, 2022J05088) and Fujian Science & Technology Innovation Laboratory for Optoelectronic Information of China (2021ZR101).

Notes and references

- C. Tang, R. Zhang, W. Lu, L. He, X. Jiang, A. M. Asiri and X. Sun, *Adv. Mater.*, 2017, **29**, 1602441.
- Z. Xue, K. Liu, Q. Liu, Y. Li, M. Li and C. Y. Su, *Nat. Commun.*, 2019, **10**, 5048.
- C. Tang, R. Zhang, W. Lu, Z. Wang, D. Liu, S. Hao, G. Du, A. M. Asiri and X. Sun, *Angew. Chem., Int. Ed.*, 2017, **56**, 842–846.
- L. Xie, X. Li, B. Wang, J. Meng, H. Lei, W. Zhang and R. Cao, *Angew. Chem., Int. Ed.*, 2019, **58**, 18883–18887.
- M. S. Yao, W. X. Tang, G. E. Wang, B. Nath and G. Xu, *Adv. Mater.*, 2016, **28**, 5229–5234.
- Y. P. Zhu, T. Y. Ma, M. Jaroniec and S. Z. Qiao, *Angew. Chem., Int. Ed.*, 2017, **56**, 1324–1328.
- T. H. Yang, K. C. Chiu, Y. W. Harn, H. Y. Chen, R. F. Cai, J. J. Shyue, S. C. Lo, J. M. Wu and Y. H. Lee, *Adv. Funct. Mater.*, 2018, **28**, 1706113.
- K. Ramanathan, M. A. Bangar, M. Yun, W. Chen and N. V. Myung, *J. Am. Chem. Soc.*, 2005, **127**, 496–497.
- W. Han, H. He, L. Zhang, C. Dong, H. Zeng, Y. Dai, L. Xing, Y. Zhang and X. Xue, *ACS Appl. Mater. Interfaces*, 2017, **9**, 29526–29537.
- X. Ji, C. Xiao, W. F. Lau, J. Li and J. Fu, *Biosens. Bioelectron.*, 2016, **82**, 240–247.
- J. Chai and J. M. Buriak, *ACS Nano*, 2008, **2**, 489–501.
- W. Lu, P. Gao, W. B. Jian, Z. L. Wang and J. Fang, *J. Am. Chem. Soc.*, 2004, **126**, 14816–14821.
- C. Zhu, Y. He, Y. Liu, N. Kazantseva, P. Saha and Q. Cheng, *J. Energy Chem.*, 2019, **35**, 124–131.
- C. Hu, L. Chen, Y. Hu, A. Chen, L. Chen, H. Jiang and C. Li, *Adv. Mater.*, 2021, **33**, 210355.
- H. Duan, Z. Zhao, J. Lu, W. Hu, Y. Zhang, S. Li, M. Zhang, R. Zhu and H. Pang, *ACS Appl. Mater. Interfaces*, 2021, **13**, 33083–33090.
- J. Liu, Z. Luo, X. Mao, Y. Dong, L. Peng, D. Sun-Waterhouse, J. V. Kennedy and G. I. N. Waterhouse, *Small*, 2022, **18**, 2204553.
- L. Chen, D. Jiang, X. Liu and G. Qiu, *ChemPhysChem*, 2014, **15**, 1624–1631.
- S. S. A. Abdul Haroon Rashid, Y. M. Sabri, A. E. Kandjani, C. J. Harrison, R. K. Canjeevaram Balasubramanyam, E. Della Gaspera, M. R. Field, S. K. Bhargava, A. Tricoli, W. Wlodarski and S. J. Ippolito, *ACS Appl. Mater. Interfaces*, 2019, **11**, 29255–29267.
- M. Yan, N. Yu, S. Du, H. Li and Y. Wu, *Bull. Mater. Sci.*, 2022, **45**, 105.
- J. Liu, R. Lu, G. Xu, J. Wu, P. Thapa and D. Moore, *Adv. Funct. Mater.*, 2013, **23**, 4941–4948.
- M. Reches and E. Gazit, *Nat. Nanotechnol.*, 2006, **1**, 195–200.
- M. Schwartzman, D. Tsvion, D. Mahalu, O. Raslin and E. Joselevich, *Proc. Natl. Acad. Sci. U. S. A.*, 2013, **110**, 15195–15200.
- D. Tsvion, M. Schwartzman, P. Popovitz-Biro, P. von Huth and E. Joselevich, *Science*, 2011, **333**, 1003–1007.
- D. Tsvion, M. Schwartzman, R. Popovitz-Biro and E. Joselevich, *ACS Nano*, 2012, **6**, 6433–6445.
- D. Dávila, A. Tarancón, C. Calaza, M. Salleras, M. Fernández-Regúlez, A. San Paulo and L. Fonseca, *Nano Energy*, 2012, **1**, 812–819.
- C. Geng, Y. Jiang, Y. Yao, X. Meng, J. A. Zapien, C. S. Lee, Y. Lifshitz and S. T. Lee, *Adv. Funct. Mater.*, 2004, **14**, 589–594.
- S. Xu, Y. Ding, Y. Wei, H. Fang, Y. Shen, A. K. Sood, D. L. Polla and Z. L. Wang, *J. Am. Chem. Soc.*, 2009, **131**, 6670–6671.
- M. M. Yusoff, M. H. Mamat, A. S. Ismail, M. F. Malek, A. S. Zoofakar, A. B. Suriani, M. K. Ahmad, N. Nayan, I. B. Shameem Banu and M. Rusop, *J. Mater. Sci.*, 2018, **30**, 1017–1033.
- V. V. Burungale, V. V. Satale, A. J. More, K. K. K. Sharma, A. S. Kamble, J. H. Kim and P. S. Patil, *J. Colloid Interface Sci.*, 2016, **470**, 108–116.
- R. Bhardwaj and A. Hazra, *ACS Appl. Nano Mater.*, 2022, **5**, 15507–15517.
- Z. Lu, C. T. Yip, L. Wang, H. Huang and L. Zhou, *ChemPlusChem*, 2012, **77**, 991–1000.
- R. Cristina, M. Olga, S. Alejandra, M. Guillermo, G. Ana, R. Patrick, K. Thomas, M. IbrahimDar, K. N. Mohammad and J. B. Henk, *Energy Environ. Sci.*, 2014, **7**, 994–997.
- L. Z. Liu, W. Xu, X. L. Wu, Y. Y. Zhang, T. H. Chen and P. K. Chu, *Appl. Phys. Lett.*, 2012, **100**, 121904.
- F. Wu, X. Hu, J. Fan, E. Liu, T. Sun, L. Kang, W. Hou, C. Zhu and H. Liu, *Plasmonics*, 2012, **8**, 501–508.
- C. Mercado, Z. Seeley, A. Bandyopadhyay, S. Bose and J. L. McHale, *ACS Appl. Mater. Interfaces*, 2011, **3**, 2281–2288.
- T. Gakhar and A. Hazra, *J. Electron. Mater.*, 2019, **48**, 5342–5347.
- S. Mondal and D. Basak, *J. Lumin.*, 2016, **179**, 480–486.
- T. P. Hardcastle, R. M. D. Brydson, K. J. T. Livi, C. R. Seabourne and A. J. Scott, *J. Phys.: Conf. Ser.*, 2012, **371**, 012059.
- H. Perron, C. Domain, J. Roques, R. Drot, E. Simoni and H. Catalette, *Theor. Chem. Acc.*, 2007, **117**, 565–574.
- W. Guo, W. Zhang, N. Han, S. Xie, Z. Zhou and W. Monnens, *Chem.–Eur. J.*, 2023, **29**, e202302338.
- C. N. Yeh, Y. M. Chen, C. A. Chen, Y. S. Huang, D. S. Tsai and K. K. Tiong, *Thin Solid Films*, 2010, **518**, 4121–4125.
- C. C. Chen, R. S. Chen, T. Y. Tsai, Y. S. Huang, D. S. Tsai and K. K. Tiong, *J. Phys.: Condens. Matter*, 2004, **16**, 8475–8484.
- R. S. Chen, A. Korotcov, Y. S. Huang and D. S. Tsai, *Nanotechnology.*, 2006, **17**, 67–87.
- F. D. Qu, S. D. Zhang, C. Z. Huang, X. Y. Guo, Y. Zhu, T. J. Thomas, H. C. Guo, J. P. Attfield and M. H. Yang, *Angew. Chem., Int. Ed.*, 2021, **60**, 6561–6566.
- X. L. Ye, S. J. Lin, J. W. Zhang, H. J. Jiang, L. A. Cao, Y. Y. Wen, M. S. Yao, W. H. Li, G. E. Wang and G. Xu, *ACS Sens.*, 2021, **6**, 1103–1110.

- 46 J. Z. Xiao, Z. H. Fu, G. E. Wang, X. L. Ye and G. Xu, *Chin. J. Struct. Chem.*, 2022, **41**, 2204054–2204060.
- 47 J. Nowotny, T. Bak, L. R. Sheppard and M. K. Nowotny, *J. Am. Chem. Soc.*, 2008, **130**, 9984–9993.
- 48 P. Feng, Q. Wan and T. H. Wang, *Appl. Phys. Lett.*, 2005, **87**, 213111.
- 49 Y. Qin, Z. Cui, T. Zhang and D. Liu, *Sens. Actuators, B*, 2018, **258**, 246–254.
- 50 A. Hazra, B. Bhowmik, K. Dutta, P. P. Chattopadhyay and P. Bhattacharyya, *ACS Appl. Mater. Interfaces*, 2015, **7**, 9336–9348.
- 51 A. Hazra, K. Dutta, B. Bhowmik, P. P. Chattopadhyay and P. Bhattacharyya, *Appl. Phys. Lett.*, 2014, **105**, 081604.
- 52 B. Bhowmik and P. Bhattacharyya, *RSC Adv.*, 2015, **5**, 82159–82168.
- 53 N. Zhang, G. Ren, L. Li, Z. Wang, P. Yu and X. Li, *Nat. Commun.*, 2024, **15**, 2777.
- 54 S. Blomberg, U. Hejral, M. Shipilin, S. Albertin, H. Karlsson, C. Hulteberg, P. Lömkker, C. Goodwin, D. Degerman, J. Gustafson, C. Schlueter, A. Nilsson, E. Lundgren and P. Amann, *ACS Catal.*, 2021, **11**, 9128–9135.
- 55 *Convention on Road Traffic of 1968 and European Agreement Supplementing the Convention: 2006 Consolidated Versions*, United Nations, New York, 2007.